nature physics

LETTERS

https://doi.org/10.1038/s41567-019-0651-0

Corrected: Author Correction

Enhancement of interlayer exchange in an ultrathin two-dimensional magnet

Dahlia R. Klein[1,8], David MacNeill[1,8], Qian Song[2], Daniel T. Larson[3], Shiang Fang[3], Mingyu Xu[4,5], R. A. Ribeiro[4,5,6], P. C. Canfield[4,5], Efthimios Kaxiras[3,7], Riccardo Comin[1] and Pablo Jarillo-Herrero[1*]

Following the recent isolation of monolayer CrI_3 (ref. [1]), many more two-dimensional van der Waals magnetic materials have been isolated[2–12]. Their incorporation in van der Waals heterostructures offers a new platform for spintronics[5–9], proximity magnetism[13] and quantum spin liquids[14]. A primary question in this field is how exfoliating crystals to the few-layer limit influences their magnetism. Studies of CrI_3 have shown a different magnetic ground state for ultrathin exfoliated films[1,5,6] compared with the bulk, but the origin is not yet understood. Here, we use electron tunnelling through few-layer crystals of the layered antiferromagnetic insulator $CrCl_3$ to probe its magnetic order and find a tenfold enhancement of the interlayer exchange compared with bulk crystals. Moreover, temperature- and polarization-dependent Raman spectroscopy reveals that the crystallographic phase transition of bulk crystals does not occur in exfoliated films. This results in a different low-temperature stacking order and, we hypothesize, increased interlayer exchange. Our study provides insight into the connection between stacking order and interlayer interactions in two-dimensional magnets, which may be relevant for correlating stacking faults and mechanical deformations with the magnetic ground states of other more exotic layered magnets such as $RuCl_3$ (ref. [14]).

The layered transition metal trihalides are an important family of van der Waals magnets and have been studied for decades as prototypical magnetic insulators[15,16] and as a platform for quasi-two-dimensional magnetism[17,18]. In the chromium trihalides, the chromium atoms are arranged in a honeycomb structure, with each chromium atom surrounded by six halide atoms in an octahedral geometry (Fig. 1a). The bulk crystals undergo a crystallographic phase transition from a monoclinic phase (space group $C2/m$) at room temperature to a rhombohedral phase (space group $R\bar{3}$) at low temperatures (below about 240 K for $CrCl_3$ (ref. [19])). While the intralayer lattice spacings are largely unaffected by this transition, the layer stacking sequence changes from rhombohedral ABC ordering at low temperatures to $AA_{1/3}$ stacking above 240 K, where each layer is displaced along the a axis by 1/3 of a lattice vector (Fig. 1a). Bulk CrI_3 and $CrBr_3$ are ferromagnetic (FM) below their Curie temperatures, with moments aligned perpendicular to the ab plane; in contrast, bulk $CrCl_3$ is antiferromagnetic (AFM) below its Néel temperature (T_N) of 14 K (refs. [19–21]). The chromium moments in each layer of $CrCl_3$ are ferromagnetically coupled, but couple antiferromagnetically across the van der Waals gap (Fig. 1b). However, this interlayer exchange coupling is weak, and the magnetization of adjacent layers in bulk $CrCl_3$ can be aligned with a small in-plane magnetic field, $\mu_0 H_{\parallel}$, of about 0.2–0.25 T (refs. [19,22]).

The nature of stacking in few-layer chromium trihalides has recently attracted attention because of the observation of an AFM ground state and interlayer exchange in few-layer CrI_3, in contrast to the FM ground state of bulk crystals[1,3,5,6,23,24]. This crossover from FM to AFM interlayer coupling has led to theoretical investigations centred on the origin of the AFM ground state in bilayer CrI_3[25–27]. First-principles calculations predict that while the rhombohedral phase favours FM interlayer exchange, the monoclinic phase prefers an AFM alignment between the layers[27]. Thus, it is natural to propose that the observed AFM coupling results from a monoclinic stacking that persists to low temperatures in ultrathin CrI_3. However, this proposal has not been verified experimentally. For $CrCl_3$, both the crystal and magnetic structures of ultrathin films are unknown and could provide valuable insight into how stacking order and exfoliation couple to interlayer interactions in these materials.

In this work, we use electron tunnelling to probe the magnetic structure and interlayer exchange coupling of few-layer $CrCl_3$ crystals. We first use mechanical exfoliation to obtain crystallites ranging from two to four layers in thickness. We then fabricate vertical magnetic tunnel junctions using two few-layer graphite electrodes above and below each $CrCl_3$ flake and encapsulated with hexagonal boron nitride (Fig. 1c, see Methods). In the final step, each stack is transferred onto a silicon substrate with a 285 nm oxide layer and prepatterned titanium/palladium (Ti/Pd) wires contacting the graphite electrodes. The junctions show a high resistance (Fig. 1d and Supplementary Information) with a nonlinear current–voltage (I–V) relationship characteristic of tunnelling in the Fowler–Nordheim regime[28].

We find that the junction conductance increases when a magnetic field is applied in the plane of the crystal layers. Figure 2a shows the differential conductance for a tetralayer device as a function of bias, at 300 mK and with in-plane applied fields of 0 T and 2 T, where the a.c. excitation is 50 mV. The junction differential magnetoresistance

$$\mathrm{MR} = \frac{\frac{\mathrm{d}I}{\mathrm{d}V}\left(\mu_0 H_{\parallel}\right) - \frac{\mathrm{d}I}{\mathrm{d}V}\left(\mu_0 H_{\parallel} = 0\right)}{\frac{\mathrm{d}I}{\mathrm{d}V}\left(\mu_0 H_{\parallel} = 0\right)} \times 100\% \qquad (1)$$

is plotted in Fig. 2b, where μ_0 is the permeability of free space, and $\mu_0 H_{\parallel} = 2$ T for the high-field measurement. Note that our definition

[1]Department of Physics, Massachusetts Institute of Technology, Cambridge, MA, USA. [2]Department of Materials Science and Engineering, Massachusetts Institute of Technology, Cambridge, MA, USA. [3]Department of Physics, Harvard University, Cambridge, MA, USA. [4]Ames Laboratory, US Department of Energy, Iowa State University, Ames, IA, USA. [5]Department of Physics and Astronomy, Iowa State University, Ames, IA, USA. [6]Centro de Ciências Naturais e Humanas, Universidade Federal do ABC, Santo André, Brazil. [7]John A. Paulson School of Engineering and Applied Sciences, Harvard University, Cambridge, MA, USA. [8]These authors contributed equally: Dahlia R. Klein, David MacNeill. *e-mail: pjarillo@mit.edu

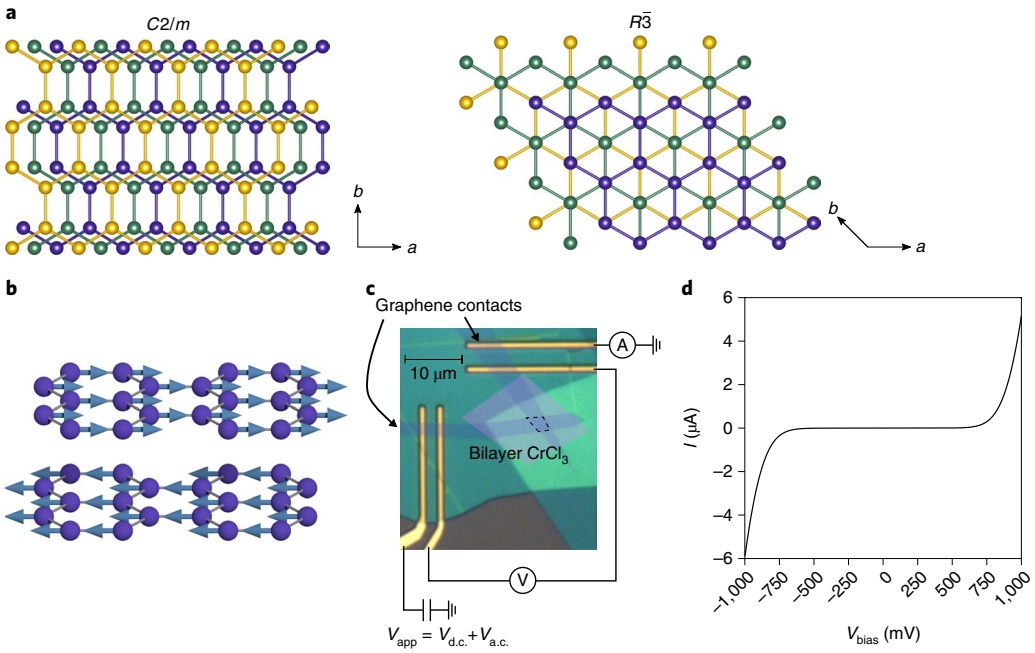

Fig. 1 | $CrCl_3$ stacking order and device characteristics. a, Stacking sequence of the chromium honeycomb sublattice in the *C2/m* (high temperature, left) and $R\bar{3}$ (low temperature, right) phases of $CrCl_3$, viewed perpendicular to the *ab* plane. The coloured spheres represent Cr^{3+} ions in three adjacent layers. In both cases, the first and fourth layers are approximately aligned. **b**, Schematic of moments in two adjacent layers at equilibrium. The moments lie in the *ab* plane. **c**, False-colour optical microscope image of a bilayer $CrCl_3$ tunnel junction device with four-point contact geometry for differential conductance measurements (V_{app}, applied voltage; $V_{d.c.}$, d.c. voltage; $V_{a.c.}$, a.c. voltage). **d**, Current versus bias voltage (V_{bias}) for a trilayer tunnel junction at 4.2 K. The current was obtained by integration of the differential conductance with an a.c. bias voltage excitation of 50 mV.

of MR is mathematically equivalent to $(R_{LO}-R_{HI})/R_{HI}$, where R_{HI} and R_{LO} refer to resistances with and without an applied magnetic field, respectively. Consistent with previous results[6] and the theory of spin filter tunnelling[29], the differential magnetoresistance peaks at a finite bias value near the onset of Fowler–Nordheim tunnelling (between 625 mV and 875 mV). This peak corresponds to a maximum of spin-polarized tunnelling when the applied bias is sufficient to allow efficient Fowler–Nordheim tunnelling for majority-spin electrons, which experience a lower energy barrier in the $CrCl_3$ when it is polarized, but not for minority-spin electrons, which experience a larger energy barrier. We investigate the temperature and field dependence of this phenomenon by plotting the tunnelling conductance of a $CrCl_3$ bilayer device as a function of both magnetic field and temperature (Fig. 2c). A vertical line cut of conductance versus temperature at zero applied field (Fig. 2d) shows a marked decrease in the conductance between 15 K and 16 K. This drop reflects the onset of AFM alignment between the two layers in the junction, similar to the bulk Néel temperature[19]. If the interlayer exchange were FM instead, we would expect increased conductance in the magnetic state due to the lowering of the energy barrier for majority-spin electrons[28].

In principle, two mechanisms can provide magnetoresistance in our junctions: increasing the saturation magnetization within each layer (which decreases the majority-spin barrier[30]), and rotation of the magnetization in adjacent layers from antiparallel to parallel as the external field is increased (called the double spin filter effect[29,31]). We expect that the latter effect is dominant in our junctions because (1) the observed Néel temperature is similar to bulk crystals, in which case, the magnetization in each layer is nearly saturated at $3\mu_B$ per chromium atom by 10 K, and (2) we observe only a single kink in the conductance versus magnetic field curves, rather than the two that would be expected for an alignment of the layers followed by a saturation of the intralayer magnetization.

To analyse our conductance versus applied magnetic field data at 4.2 K, and to extract the interlayer exchange, we model the magnetization as fully saturated within each layer and coupled between layers via an AFM exchange field, H_E (see Supplementary Information for the precise definition of our model and interlayer exchange field). The experimental magnetoresistance curves are shown in Fig. 3a. Consistent with the spin filter effect when tunnelling through a magnetic insulating barrier[31,32], the magnetoresistance increases with barrier thickness from 9% in a bilayer $CrCl_3$ device up to 208% in a tetralayer $CrCl_3$ device (Fig. 3c). The normalized magnetoresistance curves are displayed in Fig. 3b to emphasize the difference in saturation fields. In all devices, the AFM to FM transition occurs at a much higher field than for bulk crystals (roughly 0.2–0.25 T)[19,22]. These AFM–FM transition fields range from 0.85 T in the bilayer junction to 1.65 T in the tetralayer junction. The reported bulk interlayer exchange field is 0.084 T (ref. [17]). However, on the basis of the saturation fields in Fig. 3a, we calculate increased values for the exchange coupling of 0.86 T, 0.96 T and 0.97 T in bilayer, trilayer and tetralayer $CrCl_3$, respectively (see Supplementary Information for calculation of the interlayer exchange from the experimentally observed metamagnetic transition). The consistency of the extracted interlayer exchange coupling for different thicknesses, despite large differences in the saturation field, supports our hypothesis that the magnetoresistance arises from alignment of magnetic moments in adjacent layers. These magnetoresistances thus demonstrate a more than tenfold increase in the interlayer exchange strength when $CrCl_3$ is cleaved to the few-layer limit. Furthermore, the thickness dependence of the interlayer exchange in the few-layer films is weak, and the interlayer exchange is seen to slightly increase with thickness in our devices. This suggests that the dramatic enhancement is due to a qualitatively different property of the exfoliated films compared with bulk (that is, their stacking order).

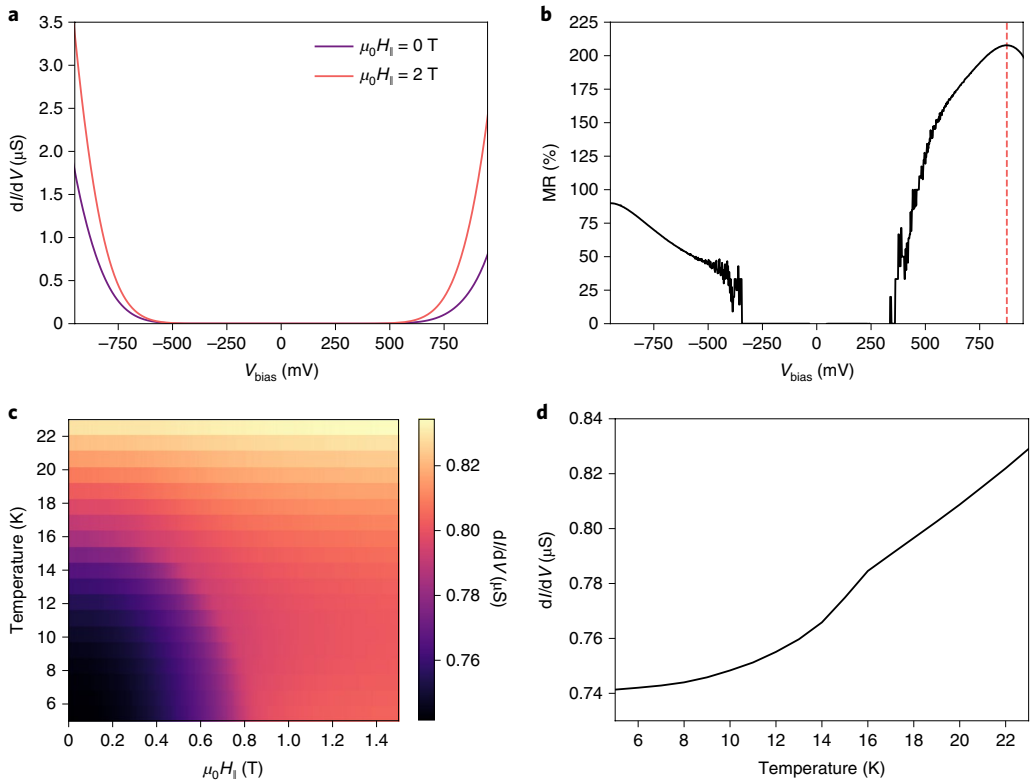

Fig. 2 | Magnetoresistance in $CrCl_3$ magnetic tunnel junctions. a, Differential conductance versus bias voltage for a tetralayer tunnel junction with an a.c. excitation of 50 mV at 300 mK. The data are taken at zero applied field (purple) and with an in-plane magnetic field of 2 T (pink). **b**, Magnetoresistance percent versus applied bias voltage for a tetralayer tunnel junction with a high-field in-plane magnetic field of 2 T, extracted from **a**. The dashed line at a bias of 875 mV indicates the optimum bias for magnetoresistance. **c**, Differential conductance versus applied in-plane magnetic field and temperature for a bilayer tunnel junction. The d.c. bias is −625 mV and the a.c. excitation is 50 mV. **d**, Vertical line cut from **c** at zero applied magnetic field. The kink between 15 K and 16 K indicates T_N.

To explore our hypothesis of stacking order as the origin of enhanced interlayer exchange, we performed Raman spectroscopy on both bulk and exfoliated thin $CrCl_3$ crystals (Fig. 4). The experiments were performed in a backscattering geometry with a 532 nm laser, incident perpendicular to the crystal *ab* plane. The incident light was linearly polarized, and inelastically scattered photons were detected in the parallel-polarized channel (XX polarization geometry). The 247 cm^{-1} Raman mode of bulk $CrCl_3$ undergoes a marked peak shift close to 2 cm^{-1} at the crystallographic phase transition near 240 K (ref. [33]). This excitation corresponds to out-of-plane vibrations of chlorine atoms in the *ab* plane, which depend sensitively on the shearing of layers with respect to one another. To calibrate the peak position, we also fit the 209 cm^{-1} Raman mode, which does not shift at the phase transition, and plot the difference between the two peak energies. We first studied the evolution of this energy difference when cooling a bulk crystal (Fig. 4a). Consistent with previous work[33], we observe a sharp shift in the peak energy difference between 240 K and 250 K (see Supplementary Information for complete spectra). Next, we examined the same peaks in an exfoliated crystal (35 nm thick) on a SiO_2/Si substrate. The peak difference shows minimal temperature dependence and no evidence of a transition, even down to 10 K (Fig. 4b). We find similar results in an even thinner (8 nm thick) exfoliated crystal, with no apparent phase transition down to 180 K (Fig. 4c). This absence of a peak shift suggests that thin exfoliated $CrCl_3$ crystals remain in the high-temperature monoclinic phase at low temperatures. Another explanation is that deformation of the crystal during the aggressive exfoliation process introduces stacking faults. In fact, repeated deformation of a bulk α-$RuCl_3$ crystal by bending back and forth gives rise to stacking faults, leading to a change in the Néel temperature[34]. Thus, the exfoliation process itself probably plays a role in modifying the physical properties of thin van der Waals crystals, compared with their original bulk structures.

To further study the crystal phases of exfoliated versus bulk $CrCl_3$, we analysed the energy of the 247 cm^{-1} Raman peak as a function of polarization angle. In the rhombohedral $R\bar{3}$ phase, this peak is produced by a doubly degenerate E_g mode, whereas in the monoclinic $C2/m$ phase, it arises from a combination of closely spaced A_g and B_g modes[35,36]. In both cases, the two modes contributing to the observed peak have opposite polarization dependence. When they are degenerate, the opposite polarization dependences of these modes cancel out, leading to a single peak with constant intensity at one energy, as seen in the $R\bar{3}$ phase. However, when the two modes are slightly offset in energy, their out-of-phase intensity variations lead to the observation of a combined peak whose position displays a fourfold modulation as a function of polarization angle (see Supplementary Information for a detailed analysis). On the basis of these symmetry arguments, we can determine the crystal structure of bulk and thin films via polarized Raman spectroscopy. For a bulk crystal at 300 K (and therefore in the $C2/m$ phase), we observe a fourfold variation in the energy of this peak as we sweep the polarization angle (Fig. 4d). However, when cooling the bulk sample to 80 K, the peak energy oscillations become an order of magnitude smaller. This change is indicative of the crystallographic phase transition to the $R\bar{3}$ phase by 80 K (the small, resolution-limited residual signal may arise from some regions pinned in the high-temperature structure; see ref. [20]). In contrast, we found that a thin (17 nm thick)

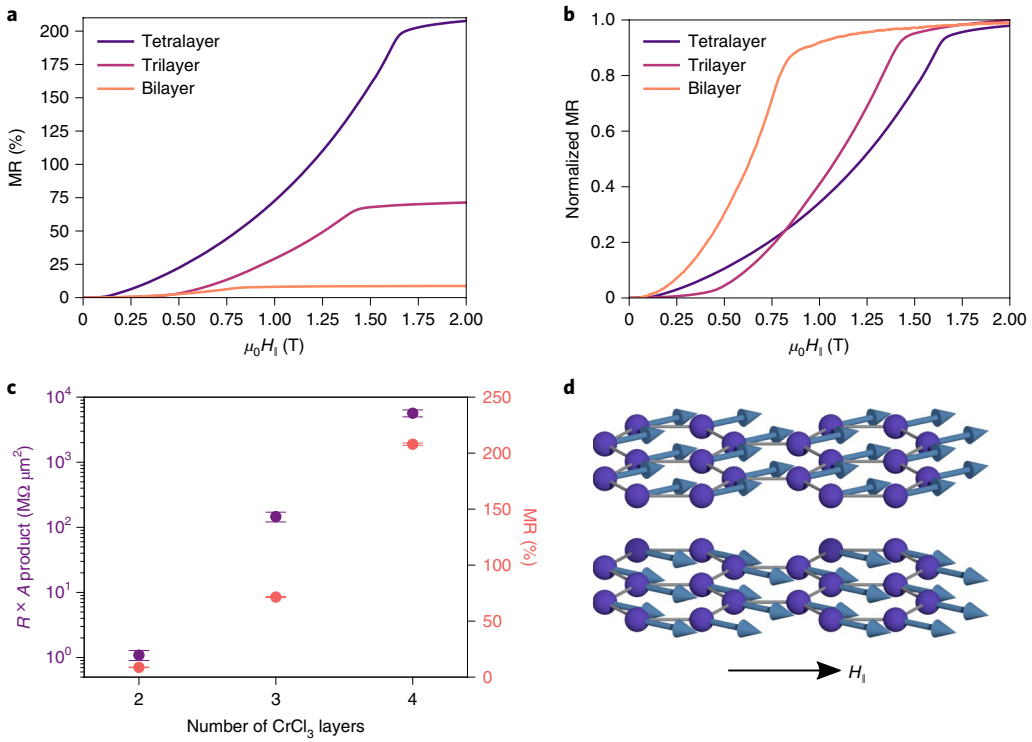

Fig. 3 | Thickness dependence of $CrCl_3$ magnetic tunnel junctions. a, Magnetoresistance versus applied in-plane magnetic field for bilayer, trilayer and tetralayer tunnel junctions at finite applied bias and an a.c. excitation of 50 mV at 4 K. **b**, Normalized magnetoresistance versus applied in-plane magnetic field, obtained by dividing the value by the MR value at 2 T. **c**, Differential resistance–area ($R \times A$) product (purple) and magnetoresistance (pink) versus $CrCl_3$ layer number. The differential resistance was measured with an applied d.c. bias of 500 mV at 4 K for each device. Error bars in the differential resistance–area product and magnetoresistance represent estimated standard deviations arising from calculation of junction areas from optical microscope images and estimation of magnetoresistance plateaus, respectively. **d**, Schematic of moments in two layers canting towards the in-plane applied field.

exfoliated flake on a SiO_2/Si substrate has fourfold variation in the 247 cm^{-1} mode peak position at both 300 K and 80 K (Fig. 4e). This result gives additional evidence that exfoliated $CrCl_3$ is in the monoclinic phase even at lower temperatures.

Note that the oscillation of the 247 cm^{-1} Raman peak energy in the exfoliated crystal is smaller at 80 K than at 300 K. This could arise from either a partial transition of the crystal into the low-temperature phase or some inherent temperature dependence of the peak oscillation due to inhomogeneous hardening of the closely lying phonon lines. We cannot rule out either scenario, but expect that our junctions are uniformly in the monoclinic stacking order. This is because we observe only a single kink in the magnetoresistance versus field traces, ruling out the presence of a highly non-uniform interlayer exchange coupling. In one trilayer device (see Supplementary Information), we did see a sharp increase in the magnetoresistance saturating around 0.15 T, which could arise from a stacking fault within the barrier creating coexisting regions of monoclinic and rhombohedral stacking.

To understand the dependence of the interlayer exchange on the stacking type, we carried out density functional theory (DFT) calculations of the energy difference between the FM and AFM states for bilayer $CrCl_3$ with various stacking arrangements (see Supplementary Information). We find that the $C2/m$-type stacking in the bilayer favours an AFM interlayer alignment, whereas the $R\bar{3}$-type phase can favour AFM or FM coupling, depending on the chosen DFT functional and interlayer spacing. Furthermore, the difference in interlayer exchange energy between the $C2/m$-type and $R\bar{3}$-type structures is not very sensitive to the DFT functional used and shows that the $C2/m$-type phase always has notably larger AFM coupling than the $R\bar{3}$-type phase. For a realistic range of interlayer spacings from 0.55 nm to 0.65 nm, the calculated value of the interlayer exchange difference is of the same order as our experimental estimate. Overall, our calculations show that the $C2/m$-type phase has stronger AFM interlayer coupling than the $R\bar{3}$-type phase, consistent with the observed giant enhancement of interlayer exchange in ultrathin $C2/m$ $CrCl_3$.

In summary, we have demonstrated a tenfold increase in the interlayer exchange of ultrathin $CrCl_3$ crystals. We attribute this dramatic enhancement to the monoclinic low-temperature crystal structure of exfoliated crystals. It is currently unknown whether this stacking structure is the lowest energy configuration or is a metastable state pinned by disorder introduced by the exfoliation process. The low-temperature monoclinic order even in very thick exfoliated crystals suggests that the latter explanation is correct. This result has important implications for understanding the unexpected magnetic behaviour in the ultrathin chromium trihalides. For example, the FM to AFM transition observed in ultrathin CrI_3 is probably also a result of $C2/m$ stacking in the few-layer crystals, as has been predicted from first-principles calculations[27]. We have also noticed a small increase in the Néel temperature in our devices compared with the bulk. It is important to see whether the Néel temperature can be correlated with spatially resolved changes, such as stacking faults, using electron microscopy or second-harmonic generation spectroscopy. Finally, our study opens up the possibility to modify exchange couplings in other van der Waals magnets through strain, twisting and other methods[37].

Online content

Any methods, additional references, Nature Research reporting summaries, source data, statements of code and data availability and

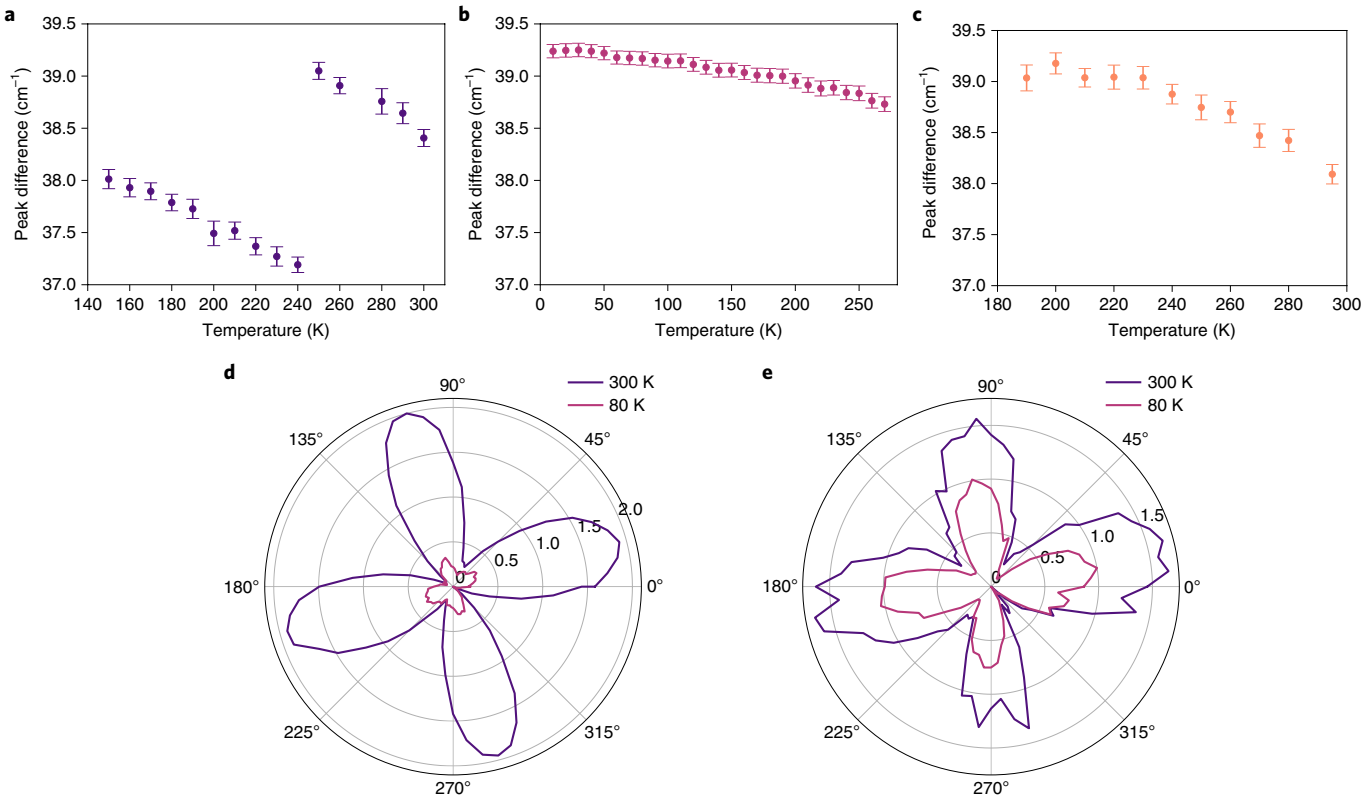

Fig. 4 | Raman spectroscopy of bulk and exfoliated $CrCl_3$. a, Difference between Raman peak positions of the 247 cm^{-1} and 209 cm^{-1} modes versus temperature for a bulk crystal of $CrCl_3$. A jump in the peak difference occurs around the crystallographic phase transition near 240 K. **b**, The same peak difference versus temperature for an exfoliated 35-nm-thick flake of $CrCl_3$ on a 90 nm SiO_2/Si substrate. The peak difference smoothly evolves down to 10 K without evidence of a phase transition. **c**, The same peak difference versus temperature for an exfoliated 8 nm flake. **d**, Peak position shift (in cm^{-1}) relative to minimum of 247 cm^{-1} mode versus polarization angle for a bulk crystal. **e**, Same as **d** for an exfoliated 17-nm-thick flake on a 90 nm SiO_2/Si substrate. All error bars reflect a 2σ confidence interval in fit parameters for the Raman peak positions.

associated accession codes are available at https://doi.org/10.1038/s41567-019-0651-0.

Received: 27 February 2019; Accepted: 29 July 2019;
Published online: 16 September 2019

References

1. Huang, B. et al. Layer-dependent ferromagnetism in a van der Waals crystal down to the monolayer limit. *Nature* **546**, 270–273 (2017).
2. Gong, C. et al. Discovery of intrinsic ferromagnetism in two-dimensional van der Waals crystals. *Nature* **546**, 265–269 (2017).
3. Huang, B. et al. Electrical control of 2D magnetism in bilayer CrI_3. *Nat. Nanotechnol.* **13**, 544–548 (2018).
4. Seyler, K. L. et al. Ligand-field helical luminescence in a 2D ferromagnetic insulator. *Nat. Phys.* **14**, 277–281 (2018).
5. Klein, D. R. et al. Probing magnetism in 2D van der Waals crystalline insulators via electron tunneling. *Science* **360**, 1218–1222 (2018).
6. Song, T. et al. Giant tunneling magnetoresistance in spin-filter van der Waals heterostructures. *Science* **360**, 1214–1218 (2018).
7. Wang, Z. et al. Very large tunneling magnetoresistance in layered magnetic semiconductor CrI_3. *Nat. Commun.* **9**, 2516 (2018).
8. Kim, H. H. et al. One million percent tunnel magnetoresistance in a magnetic van der Waals heterostructure. *Nano Lett.* **18**, 4885–4890 (2018).
9. Ghazaryan, D. et al. Magnon-assisted tunneling in van der Waals heterostructures based on $CrBr_3$. *Nat. Electron.* **1**, 344–349 (2018).
10. Kuo, C.-T. et al. Exfoliation and Raman spectroscopic fingerprint of few-layer $NiPS_3$ van der Waals crystals. *Sci. Rep.* **6**, 20904 (2016).
11. Lee, J.-U. et al. Ising-type magnetic ordering in atomically thin $FePS_3$. *Nano Lett.* **16**, 7433–7438 (2016).
12. Burch, K. S., Mandrus, D. & Park, J.-G. Magnetism in two-dimensional van der Waals materials. *Nature* **563**, 47–52 (2018).
13. Zhong, D. et al. Van der Waals engineering of ferromagnetic semiconductor heterostructures for spin and valleytronics. *Sci. Adv.* **3**, e1603113 (2017).
14. Banerjee, A. et al. Proximate Kitaev quantum spin liquid behaviour in a honeycomb magnet. *Nat. Mater.* **15**, 733–740 (2016).
15. Dillon, J. F. & Olson, C. E. Magnetization, resonance, and optical properties of the ferromagnet CrI_3. *J. Appl. Phys.* **36**, 1259–1260 (1965).
16. Cable, J. W. et al. Neutron diffraction investigation of antiferromagnetism in $CrCl_3$. *J. Phys. Chem. Solids* **19**, 29–34 (1961).
17. Narath, A. & Davis, H. L. Spin-wave analysis of the sublattice magnetization behavior of antiferromagnetic and ferromagnetic $CrCl_3$. *Phys. Rev.* **137**, A163–A178 (1965).
18. Kuhlow, B. Magnetic ordering in $CrCl_3$ at the phase transition. *Phys. Status Solidi A* **72**, 161–168 (1982).
19. McGuire, M. A. et al. Magnetic behavior and spin-lattice coupling in cleavable van der Waals layered $CrCl_3$. *Cryst. Phys. Rev. Mater.* **1**, 014001 (2017).
20. McGuire, M. A., Dixit, H., Cooper, V. R. & Sales, B. C. Coupling of crystal structure and magnetism in the layered, ferromagnetic insulator CrI_3. *Chem. Mater.* **27**, 612–620 (2015).
21. McGuire, M. A. Crystal and magnetic structures in layered, transition metal dihalides and trihalides. *Crystals* **7**, 121 (2017).
22. MacNeill, D. et al. Gigahertz frequency antiferromagnetic resonance and strong magnon–magnon coupling in the layered crystal $CrCl_3$. *Phys. Rev. Lett.* **123**, 047204 (2019).
23. Jiang, S. et al. Controlling magnetism in 2D CrI_3 by electrostatic doping. *Nat. Nanotechnol.* **13**, 549–553 (2018).
24. Thiel, L. et al. Probing magnetism in 2D materials at the nanoscale with single spin microscopy. *Science* **364**, 973–976 (2019).
25. Jiang, P. et al. Stacking tunable interlayer magnetism in bilayer CrI_3. *Phys. Rev. B* **99**, 144401 (2019).
26. Soriano, D. et al. Interplay between interlayer exchange and stacking in CrI_3 bilayers. *Solid State Commun.* **299**, 113662 (2019).
27. Sivadas, N. et al. Stacking-dependent magnetism in bilayer CrI_3. *Nano Lett.* **18**, 7658–7664 (2018).
28. Simmons, J. G. Generalized formula for the electric tunnel effect between similar electrodes separated by a thin insulating film. *J. Appl. Phys.* **34**, 1793–1803 (1963).

29. Miao, G.-X., Müller, M. & Moodera, J. S. Magnetoresistance in double spin filter tunnel junctions with nonmagnetic electrodes and its unconventional bias dependence. *Phys. Rev. Lett.* **102**, 076601 (2009).
30. Moodera, J. S., Meservey, R. & Hao, X. Variation of the electron-spin polarization in EuSe tunnel junctions from zero to near 100% in a magnetic field. *Phys. Rev. Lett.* **70**, 853–856 (1993).
31. Worledge, D. C. & Geballe, T. H. Magnetoresistive double spin filter tunnel junction. *J. Appl. Phys.* **88**, 5277–5279 (2000).
32. Hao, X., Moodera, J. S. & Meservey, R. Spin-filter effect of ferromagnetic europium sulfide tunnel barriers. *Phys. Rev. B* **42**, 8235–8243 (1990).
33. Glamazda, A. et al. Relation between Kitaev magnetism and structure in α-$RuCl_3$. *Phys. Rev. B* **95**, 174429 (2017).
34. Cao, H. B. et al. Low-temperature crystal and magnetic structure of α-$RuCl_3$. *Phys. Rev. B* **93**, 134423 (2016).
35. Bermudez, V. M. Unit-cell vibrational spectra of chromium trichloride and chromium tribromide. *Solid State Commun.* **19**, 693–697 (1976).
36. Larson, D. T. & Kaxiras, E. Raman spectrum of CrI_3: an ab initio study. *Phys. Rev. B* **98**, 085406 (2018).
37. Cao, Y. et al. Unconventional superconductivity in magic-angle graphene superlattices. *Nature* **556**, 43–50 (2018).

Acknowledgements

This work was supported by the Center for Integrated Quantum Materials under NSF grant DMR-1231319 (D.R.K., E.K. and S.F.), the DOE Office of Science, Basic Energy Sciences under award DE-SC0018935 (D.M.), as well as the Gordon and Betty Moore Foundation's EPiQS Initiative through grant GBMF4541 to P.J.-H.; D.R.K. acknowledges partial support by the NSF Graduate Research Fellowship Program under grant no. 1122374. R.C. acknowledges support from the Alfred P. Sloan Foundation. Q.S. is supported by the Xu Xin International Student Exchange Scholarship from Nanjing University. E.K. and S.F. are also supported by the ARO MURI award no. W911NF-14-0247. Work done at AmesLaboratory (M.X., R.A.R. and P.C.C.) was performed under contract no. DE-AC02-07CH11358. R.A.R. was supported by the Gordon and Betty Moore Foundation's EPiQS Initiative through grant GBMF4411. The computations in this paper were run on the Odyssey cluster supported by the FAS Division of Science, Research Computing Group at Harvard University.

Author contributions

D.R.K., D.M. and P.J.-H. conceived the project. D.R.K. and D.M. grew the bulk $CrCl_3$ crystals, fabricated and measured the transport devices and analysed the data. Q.S. carried out Raman measurements under supervision of R.C.; D.T.L. and S.F. carried out symmetry analysis and DFT calculations under supervision of E.K.; M.X., R.A.R. and P.C.C. supplied the boron nitride crystals. All authors contributed to writing the manuscript.

Competing interests

The authors declare no competing interests.

Additional information

Supplementary information is available for this paper at https://doi.org/10.1038/s41567-019-0651-0.

Reprints and permissions information is available at www.nature.com/reprints.

Correspondence and requests for materials should be addressed to P.J.-H.

Publisher's note Springer Nature remains neutral with regard to jurisdictional claims in published maps and institutional affiliations.

Methods

Bulk crystal growth. Bulk $CrCl_3$ crystals were grown by recrystallization of anhydrous $CrCl_3$ flakes. Approximately 1.0 g of the flakes (99.9%, Alfa Aesar) was loaded into a silica ampule in an inert environment and sealed under vacuum. The ampule was placed in a three-zone tube furnace with source, growth and third zones held at 700 °C, 550 °C and 625 °C, respectively, for a duration of six days. The source material was fully transported to the middle growth zone, where it recrystallized into flat platelet crystals.

Hexagonal boron nitride (hBN) single crystals were grown from a high-temperature, high-pressure solution with an atomic magnesium : boron (Mg:B) ratio of 1 : 0.7. A high-pressure and high-temperature Rockwell furnace was used to generate pressures up to 3.34 GPa and temperatures up to 1,450 °C. A 160 mg mass of $Mg_1B_{0.7}$ was put into a BN crucible, filling it to roughly 3/4 of its volume; the rest of the crucible space was filled with BN powder. The crucible and a graphite heater were then placed in the middle of a pyrophyllite cube, which was used as pressure medium for the high-pressure furnace. The assembled cube was placed into the Rockwell furnace, and pressure was applied at room temperature. After that, the growth was (1) heated to 1,450 °C over 2 h, (2) held at 1,450 °C for 1 h, (3) cooled to 650 °C over 6 h and (4) cooled to room temperature over 1 h. Once cooled, the pressure was released. The pyrophyllite cube was then broken open, and the BN crucible was removed and sealed in an evacuated amorphous silica tube for distillation of the excess Mg away from the hBN crystals. Distillation took place over 3 h, with one end of the sealed tube being held at 750 °C and the other end hanging out of a clam furnace, around 100–200 °C. After the distillation, the hBN crystals were mechanically separated from the BN crucible and MgB_2 single crystals.

Device assembly. Exfoliation of few-layer flakes from the bulk $CrCl_3$ was carried out in an argon glove box to prevent hydration of the crystals. Optical contrast was employed to determine the thickness of each flake. The van der Waals magnetic tunnel junctions were then assembled by the dry transfer process in an argon environment.

The magnetic tunnel junctions were assembled by sequentially picking up flakes of hBN, few-layer graphite, $CrCl_3$, few-layer graphite and hBN. The stacks were aligned such that the only vertical overlap between the two graphite electrodes is through the $CrCl_3$ tunnel barrier two to four layers in thickness. The use of top and bottom hBN flakes provides protection from ambient conditions and an atomically flat substrate free of dangling bonds.

In each device, the final stack was transferred onto a silicon substrate wire-bonded to a chip carrier with a 285 nm oxide layer, also containing prepatterned Ti/Pd wires. The stack was aligned so that the two few-layer graphite electrodes contact the Ti/Pd wires.

Transport measurements. Magnetotransport measurements were carried out in a helium-3 cryostat with an external magnetic field applied either parallel or perpendicular to the device. Differential conductance measurements were obtained using low-frequency lock-in methods (excitation frequency <20 Hz). Our d.c. measurements were performed by applying a d.c. bias to the sample and reading out the d.c. through a current preamplifier. All measurements were performed at fixed temperature (300 mK or 4.2 K), with the exception of the temperature-dependent data shown in Fig. 2c,d.

Raman measurements. Polarized Raman experiments were performed in a backscattering geometry using a confocal microscope spectrometer (Horiba Evolution) with a ×50 objective lens and 532 nm laser with a power of 2.0 mW. The spectrometer integration times were 5 min and 30 min for bulk and exfoliated crystals, respectively. Each scan was taken twice and then averaged before analysis.

The incident laser beam was linearly polarized in the vertical direction, and a half-wave plate was placed just before the objective. The analyser was placed in front of the spectrometer entrance and kept vertical for parallel configuration (XX). For polarization dependence, the half-wave plate was rotated in steps of 2.5° from 0° to 180°.

DFT calculations. Spin-polarized DFT calculations were performed using projector augmented-wave pseudopotentials[38] as implemented in the VASP (Vienna Ab Initio Simulation Package)[39,40]. The energy cut-off for the plane wave basis was set at 350 eV with a 17 × 17 × 1 gamma-point-centred *k*-point grid. The chlorine pseudopotential had 7 valence electrons ($3s^23p^5$), and chromium pseudopotentials with either 6 or 12 valence electrons were used ($3d^54s^1$ or $3p^63d^54s^1$, respectively). We used several exchange–correlation functionals: local density approximation[41], Perdew–Burke–Ernzerhof approximation[42] and optB86b-vdW exchange functional[43,44] with the van der Waals correlation functional[45]. Some calculations accounted for the on-site Coulomb repulsion using the simplified, rotationally invariant LDSA + U approach introduced by ref. [46]. The Hubbard parameter *U* was set at 3 eV for chromium atoms (ref. [27]).

Data availability

The data that support the findings of this study are available at https://dataverse.harvard.edu/dataverse/crcl3.

References

38. Blöchl, P. E. Projector augmented-wave method. *Phys. Rev. B* **50**, 17953–17979 (1994).
39. Kresse, G. & Furthmüller, J. Efficient iterative schemes for ab initio total-energy calculations using a plane-wave basis set. *Phys. Rev. B* **54**, 11169–11186 (1996).
40. Kresse, G. & Furthmüller, J. Efficiency of ab-initio total energy calculations for metals and semiconductors using a plane-wave basis set. *Comput. Mater. Sci.* **6**, 15–50 (1996).
41. Perdew, J. P. & Zunger, A. Self-interaction correction to density-functional approximations for many-electron systems. *Phys. Rev. B* **23**, 5048–5079 (1981).
42. Perdew, J. P., Burke, K. & Ernzerhof, M. Generalized gradient approximation made simple. *Phys. Rev. Lett.* **77**, 3865–3868 (1996).
43. Klimeš, J., Bowler, D. R. & Michaelides, A. Chemical accuracy for the van der Waals density functional. *J. Phys. Condens. Matter* **22**, 022201 (2010).
44. Klimeš, J., Bowler, D. R. & Michaelides, A. Van der Waals density functionals applied to solids. *Phys. Rev. B* **83**, 195131 (2011).
45. Dion, M. et al. Van der Waals density functional for general geometries. *Phys. Rev. Lett.* **92**, 246401 (2004).
46. Dudarev, S. L. et al. Electron-energy-loss spectra and the structural stability of nickel oxide: an LSDA+U study. *Phys. Rev. B* **57**, 1505–1509 (1998).